RSC Advances

PAPER

View Article Online
View Journal | View Issue

Cite this: *RSC Adv.*, 2024, **14**, 6016

Investigation on the growth aspects and properties of rubidium hydrogen succinate hydrate single crystal for NLO applications†

S. Kavitha[ab] and R. Ezhil Vizhi *[a]

A novel semiorganic nonlinear optical single crystal of rubidium hydrogen succinate hydrate (RbHSH) was grown at room temperature using the slow evaporation solution growth technique (SEST) with water as a solvent for nonlinear optical applications. The grown crystal is a triclinic system with a centrosymmetric space group of $P\bar{1}$ and the compound is stabilized by intramolecular O–H–O and C–H–O bonding. FTIR spectral studies were used to determine the various functional groups present in the material. The optical transmission spectra of the grown crystal demonstrated that a transparency of 89%, with a low cut off wavelength of 240 nm and an energy band gap of 5.21 eV, which is beneficial to developing advanced photonic and optoelectronic devices in the solar blind UV area. The grown crystal is thermally stable upto 174 °C. The electrical properties of RbHSH crystal exhibit low dielectric loss and a low dielectric constant at high frequencies tends to have good optical characteristics. Mechanical analysis demonstrated that the grown crystal shows the normal indentation size effect (ISE) and falls into the hard material category with $n = 1.4$. Photoconductivity measurements revealed negative photoconductivity. Photoluminescence studies showed that RbHSH emits blue light with a wavelength of 484 nm. Hirshfeld surface analysis was used to analyze intermolecular interactions in the RbHSH crystal. The grown RbHSH crystal piezoelectric charge coefficient have been calculated (d_{33} = 13 pC N^{-1}) and it is suitable for piezoelectric device applications. Under continuous-wave laser excitation, the third order nonlinear refractive index (n_2), absorption coefficient (β), and susceptibility ($\chi^{(3)}$) of the RbHSH crystal were found to be 1.6639 × 10^{-12} (cm^2 W^{-1}), 1.1739 × 10^{-5} (cm W^{-1}) and 4.86331 × 10^{-9} esu, respectively.

Received 6th November 2023
Accepted 10th January 2024

DOI: 10.1039/d3ra07579f

rsc.li/rsc-advances

Introduction

In recent years, a massive worldwide effort has been made to synthesize and grow highly effective NLO materials because NLO materials are technologically fundamental pillars of electronic and photonic industries. The structure–property relationship is the most important factor in developing an efficient NLO crystal.[1] Single crystals are important pillars of modern science and technology because they are required in numerous fields such as telecommunication, optical modulation, optoelectronics, and optical switching devices.[2,3] NLO materials will be essential components in future photonic technology. NLO applications depend on the various properties of materials, such as transparency, birefringence, refractive index, and dielectric constant as well as thermal, photochemical, and chemical stabilities.[4] Initially, research was primarily focused on pure organic and inorganic materials, which had limitations in real time applications. Organic materials are crystalline, have a low impurity content, and have an excellent structural order. In addition, they have superior optical properties to inorganic materials, particularly exceptional NLO properties with fast and large nonlinear responses across a wide frequency range.[5] However, the use of organic materials in the fabrication of industrial devices is hampered by their poor mechanical strength, low resistance to laser-induced damage, insufficient transparency, inability to grow to large sizes, and poor thermal strength. Inorganic materials, in contrast, have higher mechanical and thermal strength but have relatively poor NLO properties due to the lack of π electron delocalization. To overcome these difficulties, a new class of hybrid crystalline frameworks have been proposed and this type of material shows high stability, large nonlinearity, and good thermal and mechanical behaviour through the use of a suitable precursor, resulting in the formation of a favourable semiorganic NLO crystal. Moreover, polarizable organic molecules form bonds

[a]*Materials Research Laboratory, Centre for Functional Materials, Vellore Institute of Technology, Vellore 632014, Tamil Nadu, India. E-mail: revizhi@gmail.com; rezhilvizhi@vit.ac.in*

[b]*Department of Physics, School of Advanced Sciences, Vellore Institute of Technology, Vellore 632014, Tamil Nadu, India*

† Electronic supplementary information (ESI) available. CCDC 2297951. For ESI and crystallographic data in CIF or other electronic format see DOI: https://doi.org/10.1039/d3ra07579f

with inorganic hosts. In the acid–base interaction system of organic and inorganic molecules, highly polarizable cations with non centrosymmetric structures are responsible for NLO properties. In organic NLO materials, the fundamental structure is based on a delocalized π–π*electron system and π-bond system, in which the behaviour of molecules is triggered by a strong donor–acceptor intermolecular interaction. In addition, the properties of materials can be improved through the use of design strategies such as donor–acceptor–donor (D–A–D), donor–donor (D–D), donor–acceptor (D–A), and acceptor–donor–acceptor (A–D–A), respectively. Mainly succinic acid exists in two states: neutral as succinic acid and ionised as succinate. It creates strong intramolecular hydrogen bonds with other molecules in its ionized state.[5,6] In terms of their third-order nonlinear optical properties, metal complexes comparable to organic compounds have several benefits.[6] Due to their high nonlinearity and synthetic flexibility, organic NLO single crystals are the subject of intensive study in an attempt to meet all the mentioned technical requirements.

In 1992, Nicolone Kalsbeek reported that the crystal structure of rubidium hydrogen succinate is partially deuterated. It demonstrates the monoclinic crystal structure of space group $C2/c$. The parameter values for each cell are distinct.[7] To the best of our knowledge, rubidium hydrogen succinate hydrate (RbHSH) does not have a known crystal structure, and no one has yet performed a complete structural analysis. RbHSH, a novel nonlinear optical crystal, is described for the first time in the literature. RbHSH crystallizes in the triclinic crystal structure of space group "$P\bar{1}$" with the following cell parameters: $a = 7.86$ Å, $b = 7.86$ Å, and $c = 11.07$ Å. Using the slow evaporation technique, RbHSH single crystals of high quality and transparency were produced from an aqueous solution. RbHSH single crystal was incorporated into several characterizations, such as Powder X Ray Diffraction (PXRD), Fourier Transform Infrared (FTIR), Thermo Gravimetric/Differential Thermal Analyser (TG-DTA), optical study, dielectric study, mechanical study, Hirshfeld Surface analysis (HS), photoconductivity, refractive index, piezoelectric, Atomic Force Microscopy (AFM), and nonlinear optical study.

Synthesis and crystal growth

Equimolar ratio of the RbHSH compound was synthesized using the solution growth technique. Commercially purchased AR-grade rubidium hydroxide hydrate and succinic acid were used as starting materials. A calculated amount of material was dissolved in double distilled water. First, the amount of succinic acid was dissolved in double distilled water. Rubidium hydroxide hydrate was then progressively added to the solution and swirled thoroughly using a temperature controlled magnetic stirrer to create a homogeneous solution mixture. After getting a homogeneous solution it was filtered by using Whatman filter paper and transferred into a Petri dish and covered by a thick polythene sheet with small holes to evaporate the water molecules at room temperature. After a span of 20 days transparent colorless seed crystals were harvested in different sizes from the Petri dish, and it is represented in Fig. 1a. The morphology of RbHSH was drawn using WinX-Morph software and it is exhibited in Fig. 1b.

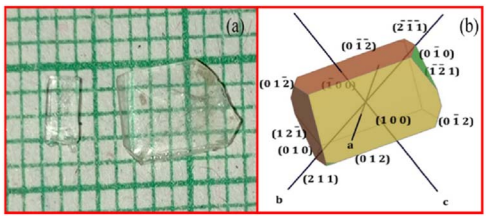

Fig. 1 (a) As grown crystal of RbHSH & (b) morphology of RbHSH crystal.

Characterization

Various characterization techniques were used on the grown crystal of RbHSH, including powder X-ray diffraction, single crystal X-ray diffraction (SXRD), Fourier Transform Infrared (FTIR), UV-visible spectra, dielectric studies, micro hardness, Z scan, refractive index, thermal studies and AFM studies.[8] The grown good quality crystal of RbHSH was finely powdered and used for powder X-ray analysis on a Bruker D8 ADVANCE diffractometer with monochromatized CuKα radiation. The lattice unit cell parameters of the RbHSH grown crystal were measured using an Enraf Nonius CAD4-MV31 single crystal X-ray diffractometer. The FTIR spectrum was recorded in the 400–4000 cm^{-1} range using the KBr pellet technique to determine the presence of various functional groups.[9] The UV-Vis spectral analysis of the crystal has been done using a PerkinElmer Lambda 35 UV-106 spectrometer. Thermogravimetric and differential Thermal analysis (DTA) were used to determine thermal stability. Thermal analysis was performed under a nitrogen atmosphere using a Q600 SDT thermal analyser at a heating rate of 20 K min^{-1}. The numeric impedance analyzer was used to collect data on the dielectric behaviour of the material at room temperature.[10] Vickers microhardness pyramidal indentation was used to test the mechanical stability of the grown crystal. Photoconductivity investigations on RbHSH single crystals were carried out using a Keithley 485 Pico ammeter. The photoluminescence (PL) emission spectra of RbHSH crystals were measured with a fluorescence spectrophotometer (HITACHI F7000). The Hirshfeld surfaces and two-dimensional (2D) fingerprint visualizations were created with the Crystal Explorer 17 program. The piezoelectric characteristic of the grown crystal was studied by measuring the piezoelectric charge coefficient, d_{33} pC N^{-1}, with a YE2730A d_{33} meter instrument. The third order nonlinear properties of the RbHSH crystal were investigated using the Z-scan method and a 632.8 nm laser beam.

Results and discussion

Single crystal XRD analysis

The title compound's single crystal data were collected using an Enraf Nonius CAD4-MV31 single crystal X-ray diffractometer. A

specimen of $C_6H_7O_6Rb$ was used for the X-ray crystallographic analysis and the X-ray intensity data were measured ($\lambda = 0.71073$ Å). The integration of the data using a triclinic unit cell yielded a total of 11 924 reflections to a maximum θ angle of 28.28° (0.75 Å resolution), of which 2106 were independent (average redundancy 5.662, completeness = 99.7%, $R_{int} = 4.56\%$, $R_{sig} = 3.68\%$) and 1932 (91.74%) were greater than 2σ (f_2). The final cell constants were $a = 7.6763$ Å, $b = 7.9380$ Å, and $c = 8.2274$ Å. The structure was solved and refined using the Bruker SHELXTL software package. The structure is triclinic and has the centrosymmetric space group $P\bar{1}$ with $Z = 2$ for the formula unit, C6H7O6Rb. The final anisotropic full-matrix least-squares refinement on F_2 with 118 variables converged at $R_1 = 3.35\%$, for the observed data and w$R_2 = 8.42\%$ for all data. The goodness-of-fit was 1.192. The largest peak in the final difference electron density synthesis was 0.588 e^- Å^{-3} and the largest hole was −1.034 e^- Å^{-3} with an RMS deviation of 0.199 e^- Å^{-3}. Based on the final model, the calculated density was 2.039 g cm^{-3} and $F(000)$, 256 e^-. The RbHSH crystal's crystallographic data (cif file) was deposited in the CCDC with the deposition number 2297951.† The structural refinement data details are shown in Table 1. Fig. 2a shows the ORTEP diagram of the RbHSH crystal. Rubidium metal is coordinated with two oxygen atoms. The bond length of the Rb1–O2(2) is 2.827(2) Å and Rb1–O7(1) is 3.090(2) Å.

The arrangement of rubidium and succinate ions indicates that the compound under consideration is an internally linked, hydrogen-bonded ion pair and can therefore be considered a crystalline molecular compound. The asymmetric unit of rubidium hydrogen succinate hydrate the protonated carboxyl group contains a succinate anion. The succinate anion plays a crucial function in intermolecular hydrogen bonding with the rubidium residue and forms stable O–H–O and C–H–O hydrogen bonds.[11,12] Two varieties of intermolecular hydrogen-bonding patterns have been observed in the crystal packing diagram. The packing diagrams in Fig. 2b–e display the four axes a, *b*, *c*, and the 210 plane with the Laue pattern. Other refinement details of bond lengths, bond angles, hydrogen bond distance, hydrogen atomic coordinates and isotropic atomic displacements are depicted in Tables S1†–S5 in ESI files.

The bond lengths and bond angles of the formed crystal are shown in Tables S2 and S3.† Table S4† summarizes how different hydrogen bonds, such as C–H–O and O–H–O, were used to stabilize the material's three-dimensional packing and hydrogen atomic coordinates and isotropic atomic displacement parameters (Å^2) for RbHSH crystals are shown in Table S5.†

Table 1 The structural refinement data for the RbHSH crystal

Chemical formula	$C_6H_7O_6Rb$
Formula weight	260.59 g mol^{-1}
Temperature	300(2) K
Wavelength	0.71073 Å
Crystal system	Triclinic
Space group	$P\bar{1}$
Unit cell dimensions	$a = 7.6763(10)$ Å, $\alpha = 73.068$ (4) $b = 7.9380(10)$ Å, $\beta = 67.252(4)°$ $c = 8.2274(11)$ Å, $\gamma = 68.824(4)°$
Volume	424.37(10) Å^3
Z	2
Density (calculated)	2.039 g cm^{-3}
Absorption coefficient	5.829 mm^{-1}
$F(000)$	256

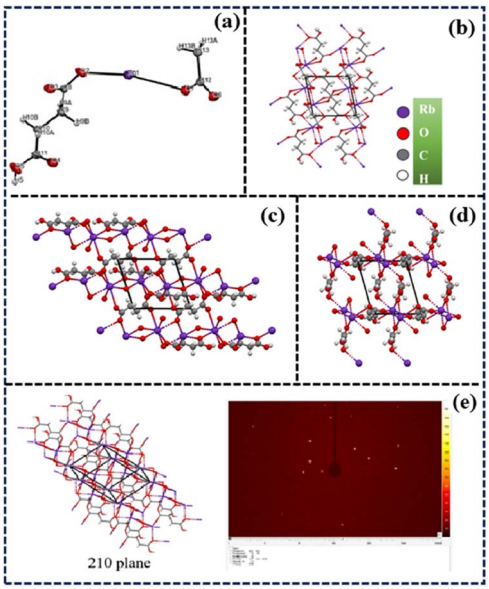

Fig. 2 (a) ORTEP diagram (b) packing diagram of *a*-axis (c) *b*-axis (d) *c*-axis (e) 210 plane and Laue pattern of RbHSH crystal.

Powder X-ray diffraction studies

RbHSH powder X-ray diffraction studies were performed with a powder X-ray diffractometer with CuKα radiation ($\lambda = 1.5460$ Å). The RbHSH crystal was crushed to a uniform fine powder and subjected to powder X-ray diffraction analysis to reveal the compound's crystalline nature.

Various structural variables, including crystallite size, dislocation density, and the number of crystallites per unit surface area, are required to obtain sufficient information about the structural transformation.[13] The average crystallite size was determined from the XRD prominent peaks using Scherrer's equation.

$$\text{Crystallite size } D = \frac{k\lambda}{\beta \cos\theta} \quad (1)$$

where λ, θ, and β represent the wavelength, Bragg's angle, and full width at half maximum, respectively. The average crystallite size of the grown material was 77.34 nm. The crystal dislocation density and number of crystallites per unit surface area (Nc) were calculated as follows:[14]

$$\text{Dislocation density } (\delta) = \frac{1}{D^2} \quad (2)$$

$$\text{Crystallites per unit surface area} = \frac{d}{D^2} \quad (3)$$

The dislocation density of the grown material is 0.000167 nm^{-2} and the number of crystallites per unit surface area is

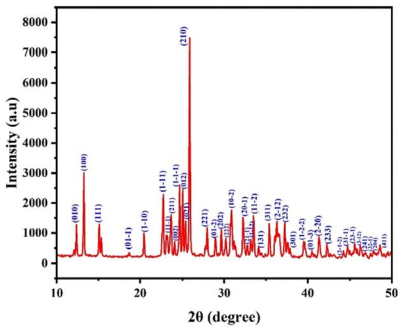

Fig. 3 Powder XRD pattern of the RbHSH crystal.

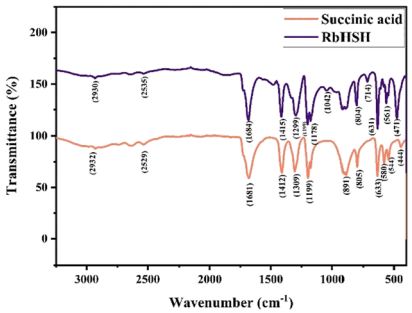

Fig. 4 FTIR spectrum of the RbHSH crystal.

calculated by using the thickness and crystallite size of the grown material. The crystallite size per unit area is 0.00216 nm^{-2}. Maximum intensity was used to record the high intensity peaks. The recorded diffraction pattern reveals the presence of all possible planes. The peak position and intensities of the diffraction provided information about the symmetry of the unit cell, atom position, and displacements of the crystalline material.[15]

Fig. 3 provides a precise depiction of the line profile shapes for the powder X-ray diffraction pattern. Using Mercury software, the corresponding (*hkl*) planes were determined by comparing the CIF file (CCDC no: 2297951†) data. Peaks were found in the planes (010), (100), (111), (01−1), (1−10), (1−11), (11−1), (211), (002), (1−1−1), (012), (021), (210), (221), (01−2), (202), (222), (10−2), (20−1), (21−1), (1−12), (11−2), (131), (311), (2−12), (232), (301), (1−2−2), (01−3), (2−20), (233), (2−1−2), (31−1), (23−1), (3−12), (241), (32−1), (204), and (411). The sharp powder XRD signals show that the crystallites are appropriately aligned and free of defects and the high intensity peaks indexed at specific 2θ angles confirmed the crystalline nature of RbHSH and the material's purity.[16]

Fourier transform infrared spectrum

The FTIR spectrum of a grown crystal was recorded using the KBr pellet technique.[17] The powdered specimen was mixed with KBr in order to form a pellet and then the powder was scanned with a spectrometer in the range between 400 cm^{-1} and 4000 cm^{-1} in order to qualitatively analyse the presence of functional groups in the grown RbHSH crystal, and the resulting spectrum is shown in Fig. 4. Using the literature, all of the peaks were assigned to the appropriate functional group. The peak at 2932 cm^{-1} is attributed to the CH_2 stretching vibration mode. The peak observed at 2535 cm^{-1} is due to atmospheric CO_2. The peak appearing at 1684 cm^{-1} is due to the presence of C=O stretching vibration.[18] The peak at 1415 cm^{-1} is attributable to symmetric stretching vibration of COO^-. Due to C–O–H bending vibration a peak was noted at 1299 cm^{-1}. The band observed at 1199–1178 cm^{-1} is due to C–O stretching vibration. The medium intensity peak observed at 1042 cm^{-1} was due to C=O bending vibration. The peak noted at 804 cm^{-1} corresponds to C–H deformation.

The metal–oxygen vibration occurred at peak 714–631 cm^{-1}. The peaks observed at 471 and 561 cm^{-1} were due to the presence of metal complexes in the material. There were additional transmittance peaks observed for Rb doped succinic acid crystals when compared with the pure phase. As a result, it confirmed that all molecules are present in the crystal structure of RbHSH. Table S6 in the ESI† data lists the various functional groups present in the compound.

UV vis spectral analysis

The absorption of UV and visible light involves the promotion of electrons in s and π orbitals from the ground state to a higher energy state; the optical transmission spectrum provides valuable information about the structure of the molecule.[19] The optical characteristic values are used in optical and optoelectronic devices such as photonic crystals, wave guides, detectors, and so on.[20] The material under consideration for NLO applications must be transparent in the wavelength region of interest.[12] The transparency of the grown crystal was 89% and it is shown in Fig. 5a that the optical absorption coefficient (α) is photon energy dependant and aids in the analysis of band structure and electron transition mode. Fig. 5b shows low absorption (240 nm) across the UV region of the grown crystal. The optical transmittance data was used to analyse the various optical characteristics. The optical absorption coefficient (α) was calculated using the well-known transmittance to absorption relationship.

$$\alpha = \frac{2.303}{t}\log\ \frac{1}{T} \tag{4}$$

where T is the transmittance and t is the thickness of the grown material. In the high energy region, the energy dependency of the absorption coefficient (α) indicates the presence of a direct band gap that corresponds to the maximum photon energy ($h\nu$).[21]

$$\alpha h\nu = A(h\nu - E_g)^{1/2} \tag{5}$$

The fundamental edge is directly related to transitions from the conduction and valence bands, and associated with direct and indirect band gaps in crystalline materials. The energy band gap of grown crystal was assessed using the Tauc's plot by creating a graph between photon energy ($h\nu$) *vs.* $(\alpha h\nu)^2$ (Fig. 5c). The slope of the fitting in Fig. 5c gives the value of Tauc parameter A. The constant A includes the information on the

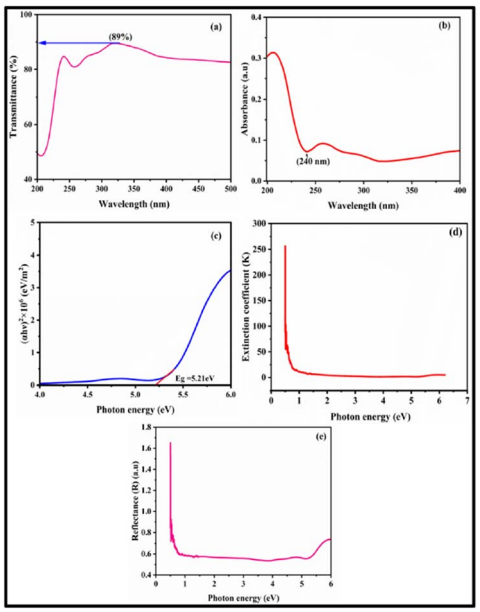

Fig. 5 (a) Transmittance, (b) absorbance, (c) Tauc's plot of RbHSH crystal, (d) extinction coefficient and (e) reflectance spectrum of RbHSH crystal.

convolution of the valence and conduction band states. This presents the matrix element of optical transitions, which reflects not only the k selection rule but also the disorder induced spatial correlation of optical transitions between the valence band and conduction band.[22,23] The band gap energy of the RbHSH crystal was calculated by extrapolating the linear portion of the curve towards the x axis.[24] It will be intercepted at 5.21 eV, indicating the bandgap energy of the RbHSH crystal.[25] The dielectric medium occurs between 3 and 6 eV, and the grown RbHSH crystal exhibits polarisation in the dielectric medium, thereby satisfying the requirements for NLO applications.[26]

Determination of optical parameters

The detailed investigation of optical constants provides an understanding of crystal optical quality, which is important for processing, adjusting, calibrating, and developing technological devices. An accurate measurement of optical properties in terms of optical parameters such as extinction coefficient (K), and reflectance (R) of the RbHSH crystal was performed.[27] The extinction coefficient value specifies the loss of electromagnetic energy produced by scattering and absorption in the crystal.[28] The measurement of the fraction of light lost due to absorption while propagating through the material was evaluated by using the relation[29]

$$K = \frac{\lambda\alpha}{4\pi} \tag{6}$$

By plotting the graph between extinction coefficient *vs.* photon energy is shown in Fig. 5d. The quantity of light lost due to scattering and absorption per unit distance of the penetrating medium that is, the minimal amount of energy lost during electromagnetic wave passage through the material is quantified by the extinction coefficient (K).[30]

A little amount of radiation was reflected from the incident radiation, and its reflectance was measured. The reflectance of the material was estimated using the thickness and absorption coefficient of the material.

$$R = \pm \frac{\sqrt{1-\exp(-\alpha t)+\exp(\alpha t)}}{1+\exp(-\alpha t)} \tag{7}$$

Fig. 5e shows the reflectance with photon energy spectrum of the grown crystal. The absorption coefficient has a significant impact on both the extinction coefficient and reflectance of the RbHSH crystal.[31] The absorption coefficient influences the internal efficiency of the device. Therefore, the perfect material for creating optoelectronic devices can be achieved by modifying the material's band gap and absorption coefficient.[32]

Thermal analysis

Thermal analysis (TGA-DTA) offers specific information on the thermal properties of the RbHSH crystal, revealing the crystal phase transition, heat stability, and solvent confirmation. At room temperature, the RbHSH crystal was crushed into uniform crystallite size and a mass of 10 mg was placed on the sample holder for TGA measurement. The yielded powder was heated from the ambient temperature to 550 °C in a nitrogen environment at a rate of 10 °C min^{-1}.[33]

Fig. 6 shows the TGA curve, revealing that there is no mass loss for the material until 174 °C. It shows that the material was thermally stable up to 174 °C. The substance begins to lose weight as the temperature rises steadily, and total disintegration occurs at 203 °C. The DTA curve indicates that there are two endothermic peaks occurring at 191 °C and 215 °C. The sharpness of the peak indicates that the crystal is exceptional crystalline quality. As a result, below its melting point, the RbHSH crystal can be employed for nonlinear applications.

Dielectric analysis

A Numeric Q Impedance Analyser was used to investigate the compound's dielectric behaviour. The dielectric studies are completed utilizing an LCR meter in the frequency scope of 50 Hz to 5 MHz.[34] The dielectric behavior provides crucial

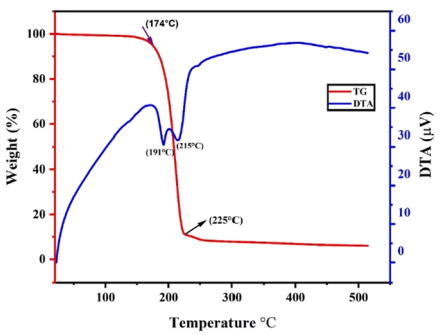

Fig. 6 TGA and DTA curves of the RbHSH crystal.

information regarding its electrical properties and this approach is used to investigate the material's charge transfer and storage capacities.[35] To improve ohmic contact, the opposite faces of the 2 mm thick RbHSH crystal were carefully coated with silver paste. The dielectric constant is essentially a measure of how easily a material may be polarised in the presence of an external electric field. The material dielectric loss and dielectric constant were measured as a function of frequency using an impedance analyser at room temperature. The dielectric loss is directly measured, and the dielectric constant is estimated using the following relation:

$$\varepsilon_r = \frac{Cd}{\varepsilon_0 A} \tag{8}$$

where c is the capacitance, d is the thickness, A is the cross section area, and ε_0 is the absolute permittivity of free space, which has the value of 8.854×10^{-12} F m^{-1}.[36] Dielectric loss in crystals is related to impurities, microstructural defects, porosity, microfractures, and uneven crystallite orientation. The dielectric loss ε' is also calculated using the relation

$$\varepsilon' = \varepsilon \tan \delta \tag{9}$$

Fig. 7a and b shows the fluctuation of dielectric constant and dielectric loss with frequency. According to the studies, the dielectric constant reduces with increasing frequency and achieves a constant value, because of the fact that the dipole does not follow the alternating field beyond a certain frequency of the electric field.

It can be attributed to the decreased electrostatic bonding strength caused by space charge polarisation near grain boundary surfaces. Fig. 7b shows that the dielectric loss greatly varies on the frequency of the applied field.[37] Dielectric loss reduces as frequency increases. The low dielectric loss with high frequency property of the RbHSH crystal possesses good optical quality with fewer flaws, and this parameter is critical for nonlinear optical materials.

Microhardness analysis

Hardness is a crucial parameter for understanding the elastic and ductile behaviour of a material. Microhardness was measured using a Mitutuoyo-HB210 Vickers microhardness tester equipped with a diamond pyramidal indenter and connected to an optical microscope. In order to get precise hardness measurements, indentations were made on the RbHSH crystal with applied loads ranging from 10 g to 90 g. The indentations were made at room temperature with a constant indentation period of 10 s. Several indentations were formed on the sample to obtain reliable findings for each given load, and the average diagonal length (d) of the indenter impressions was measured. A micrometer eyepiece was used to measure the diagonal length of the indentation mark. The following relation was used to get the microhardness value:[38]

$$H_v = \frac{1.8544\ P}{d^2}\ \text{kg mm}^{-2} \tag{10}$$

Fig. 8a depicts the fluctuation of H_v as a function of applied load for the RbHSH crystal varying from 10 g to 90 g. Cracks appear on the smooth surface above 90 g due to the discharge of internal stresses caused by the indents. It is shown that H_v decreases with increasing load, which indicates the normal indentation size effect (ISE). Mayer's law and Onitisch condition explain the relationship between the load (P) and the indentation size (d), which is given by

$$P = kd^n \tag{11}$$

where k represents the material constant and n is the Mayer index or work hardening coefficient. With the help of n value, we can identify the soft and hard material. The n value of a material measures how quickly it gains strength when it is being deformed and it can be obtained from the slope by plotting a graph between log p *vs.* log d (Fig. 8b).[39] The slope value was estimated using the linear fitting method, and the value was found to be 1.4, which is the work hardening coefficient of the material. This value confirmed that the grown RbHSH crystal belongs to the hard material category.

The yield strength of the material can be elucidated by the relation

$$\sigma y = \frac{H_v}{3} \quad \text{if} \quad n \leq 2 \tag{12}$$

Fig. 8d reveals that yield strength decreases with increasing load, implying that the formed crystal possesses considerable mechanical strength.[36]

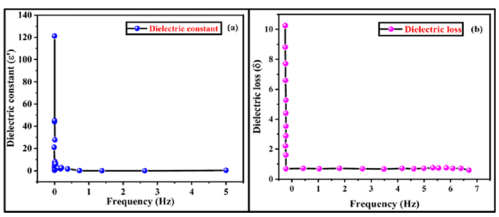

Fig. 7 (a and b) Variation of dielectric constant and dielectric loss with frequency of the RbHSH crystal.

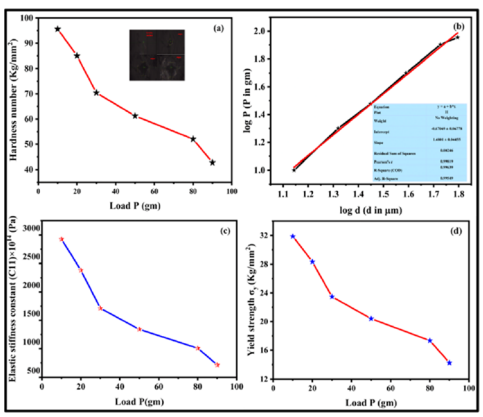

Fig. 8 (a) Plot of load *vs.* hardness number, (b) log d *vs.* log P, (c) load *vs.* elastic stiffness constant and (d) load *vs.* yield strength of RbHSH crystal.

The elastic stiffness constant explaining the Wooster's empirical relation was used to calculate the elastic stiffness constant (C_{11}).

$$C_{11} = (H_v)^{\frac{7}{4}} \quad (13)$$

The bonding information of atoms inside the material can be obtained by knowing the value of the elastic stiffness constant of the material. As shown in Fig. 8c, the elastic stiffness constant decreases with increasing load, indicating that the bonding between neighbouring atoms is strong and that the forces of attraction and repulsion between them vary with the position of the atoms.[40] The compound's elastic stiffness and yield strength were examined for a range of applied loads using the previously mentioned calculations. The mechanical parameter values are shown in Table S7 in ESI files.†

Photoconductivity studies

Photoconductivity is a very important part of photo sensors, guided guns, measuring radiation, and communicating with fibre optics. When an electric potential is given to a solid, radiation (V) shows how many photoelectrons of the solid are gained or lost. Silver paste was applied to the crystal surface to facilitate interaction between the electrodes and the crystal surface. The dark current (I_d) was elevated by delivering a voltage to the electrodes in 1 V s^{-1} steps from 0 to 50 V (DC) while preventing any radiation. The photocurrent (I_p) was measured using the same voltages (50 W halogen light).[41] The field dependency of dark and photo currents of the RbHSH crystal is shown in Fig. 9. Both dark and photo currents grow linearly with applied electric field, but the photocurrent is less than the dark current, resulting in negative photoconductivity. The sample's negative photo conductivity could be attributed to a decrease in the quantity of charge carriers in the presence of radiation.[41,42] The lower energy level has a capture cross-section for electron–hole pairs, which causes electron–hole recombination and a decrease in mobile charge carriers, resulting in negative photoconductivity.[43,44]

Photoluminescence studies

The photoluminescence spectrum indicates the presence or absence of defects and it provides information about the energy state between the valence and conduction band of grown crystals. An HITACHI F7000 Fluorescence Spectrophotometer connected to a xenon lamp and monochromator was used to investigate photoluminescence data such as excitation and emission wavelength of the title substance. The emission spectrum was observed at a excitation wavelength of 240 nm, as shown in Fig. 10a. An emission peak appears at 484 nm. The electronic transition could be caused by electron emission from an anti-bonding orbital to a bonding orbital (π*–π). The emission wavelength indicates that the grown crystal can be used in blue LED applications.

The chromaticity coordinates (x, y) of the RbHSH single crystal were calculated from the luminescence spectrum using the CIE 1931 (Commission Internationale d'Eclairage) system,

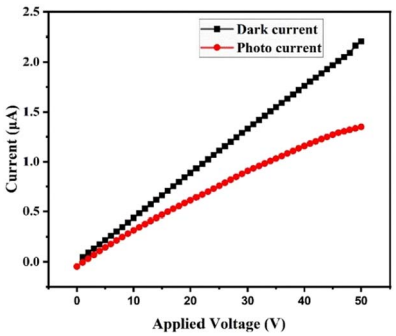

Fig. 9 Photoconductivity of the RbHSH crystal.

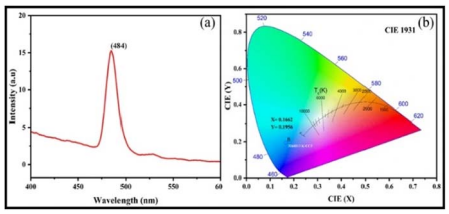

Fig. 10 (a) Photoluminescence spectrum and (b) CIE chromaticity plot of the RbHSH crystal.

as described by K. Damak *et al.* By using the emission intensities of the grown crystals are showing the colour coordinate values of x and y. The colour coordinate values (x, y) are determined to be (0.16, 0.19). It emits at a wavelength of about 484 nm. Fig. 10b shows the CIE diagram for the grown crystal, and it can be seen that the sample's x, y values emit blue light, which is suitable for light emitting diodes and display devices.[4]

Hirshfeld surface analysis

Hirshfeld surface analysis (HS) has recently emerged as a cost-effective and effective method for investigating non-covalent interactions in single crystals. The supramolecular behavior in a single crystal may be explained using Crystal Explorer 17 software.[45] HS can visualise intermolecular contacts using a colour scheme for long or short contacts. To study the RbHSH crystal, the molecular Hirshfeld surfaces are built based on the electron distribution, which is computed as the average sum of the spherical atom electron densities. The Crystal Explorer 17 software, which processes structure input files in the CIF format, was used to compute HS and their associated two-dimensional fingerprint plots that summarise all intermolecular interactions. Fig. 11a shows the d_i, d_e, d_{norm}, shape index, and curvedness of surfaces of RBHSH. It shows how curvedness and shape index surfaces are used to find out the planar stacking (π–π) interaction arrangements. Fig. 11b shows a 2-D finger map of the title chemical as well as the distribution of distances on the packing surface of one molecule in an asymmetric unit. The d_{norm} heavily relies on atom van der Waals radii, which aids in assessing the significance of intercontact of a certain site in HS utilising distinct colour coding. The major feathers of the HS plotted over d_{norm} are red, blue, and white.

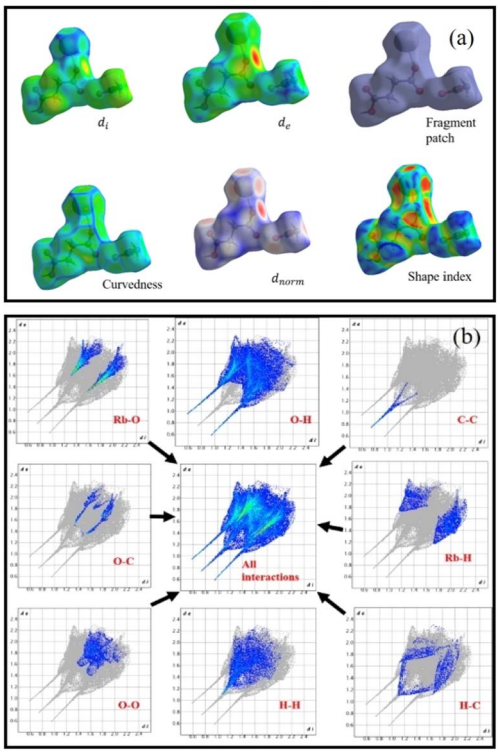

Fig. 11 (a) Hirshfeld analysis of the RbHSH material: d_i, d_e, d_{norm}, shape index, curvedness and fragment patch. (b) 2D fingerprint plots of interactions between the various elements.

The red spots on the HS represent the structures higher electron density (ED) and hydrogen bonding interaction, whereas the blue spots represent the RbHOH molecules lower ED sites. The (d_{norm}) based on d_e and d_i is defined as the distance from the surface to the external atom and internal atom to the surface, and it is calculated as follows:

$$d_{norm} = \frac{d_i - r_i^{vdw}}{r_i^{vdw}} + \frac{d_e - r_e^{vdw}}{r_e^{vdw}} \quad (14)$$

The van der Waals radius of the atom inside the HS is r_i^{vdw}, while the radius of the atom outside the HS is r_e^{vdw}. The d_{norm} was obtained a high surface resolution with a range of −1.1122 to 0.9997 Å. The intermolecular distance d_i range is 0.5958 to 2.2885 Å and d_e range is 0.5957 to 2.3335 Å. The shape index describes the distribution of electron density around the molecule surface. The intermolecular distances for shape index and curvedness are −1.0000 to 1.0000 and −4.0000 to 0.4000, and the fragment patch range is −0.0050–0.0000, respectively. Most of the organic molecule O···H, H···H and O···O intermolecular interactions are very high compared to all other interactions. Similarly, maximum and minimum intermolecular interactions that contribute to the total HS of the molecule are O···H (39.9%) and C···C (4.1%), respectively. Another major contribution of about 19.5% and 15.1% from Rb···O, H···H, Rb···H (8.4%), H···C (4.9%), O···C (4.1%) and C···C (1.2%) interactions of the total Hirshfeld surface, respectively.

Refractive index

Refractive indices have distinct relationships to the crystallographic symmetry of a crystal. Furthermore, the magnitude of the refractive indices is almost directly related to its structure. The developed crystal surface was chosen for the examination because it was free of cracks and optically clean. A few drops of methylene iodide were applied on both the prism and the crystal surface, where the prism and the crystal make close contact. Light from the lighting prism (sodium lamp) passes through the crystal and is reflected on the bottom surface of the reflector prism. A telescope was used to locate the boundary between the dark and light zones. At room temperature, the refractive index of the RbHSH crystal was determined to be 1.669.

Piezoelectric d_{33} measurements

Piezoelectric materials generate electric charge in asymmetric materials by the use of applied pressure because net dipole moments are neutralised in symmetric materials under stress.[46] Prior to measurement, the samples were coated with silver paste on opposing planes to provide adequate electrical connections and poled using a DC electric field.[47] Piezoelectric charge coefficient (d_{ij}) can be defined as

$$d_{ij} = \left(\frac{\partial D_i}{\partial T_j}\right)_E \quad (15)$$

where E, T and D are the electric field, stress, and electric displacement, respectively. The determined value of the piezoelectric charge coefficient of the crystal is 13 pC N^{-1}. A comparison of piezoelectric coefficient values is given in Table 2.[48–51]

Nonlinear optical studies

The second order nonlinear optical properties of the grown crystal were analysed using a Nd-YAG laser (1064 nm) which has

Table 2 Comparison of piezoelectric coefficients of other alkali metals[]

Crystal	Piezoelectric charge coefficient pC N^{-1}	References
Lithium sulfate monohydrate (LSMH)	6	36
Sodium acid phthalate hemihydrate	1.45	37
Potassium hydrogen phthalate	0.92	38
Ammonium dihydrogen phosphate (ADP)	1.80	39
Rubidium hydrogen succinate hydrate (RbHSH)	13	Present work

centrosymmetric nature. The input energy for the reference material (KDP) and RbHSH crystal was 0.7 joules. Due to the lack of SHG, there is no green emission of the developed material, and the output energy of KDP is 7.5 mJ. It has been concluded that centrosymmetric nature of the grown crystal dynamically obeys the third order nonlinear requirements. As a result, Sheikh Bahae *et al.* developed a simple yet extremely sensitive technique for investigating the third-order NLO characteristics of diverse optical materials. Using Z-scan analysis, optical characteristics such as third order refractive index (n_2), nonlinear absorption coefficient (β), and third order optical susceptibility ($\chi^{(3)}$) were determined for the sample. Nonlinear susceptibilities are mostly owing to the material's pure electronic effects, and most transparent materials provide nonlinearity in terms of the polarization of bound electrons.[52] In this method, the far-field intensity of a moving sample along the axis of a Gaussian beam is determined as a function of sample position.[53] In a Z-scan experiment, aperture modes such as closed and open can be used to assess the refractive index and absorption property of nonlinear materials. The closed and open apertures of the normalized transmission of the RbHSH crystal have been made as a function of sample location Z.[54] The usual eqn (13)–(15) were used to calculate the magnitude of the compound's nonlinear absorption coefficient (β), refractive index (n_2), and nonlinear susceptibility ($\chi^{(3)}$).[55] Table 3 shows the optical resolutions of the Z-scan setup and third order nonlinear parameters for the grown RbHSH crystal.

$$n_2 = \frac{\Delta\phi}{KI_0L_{\text{eff}}}\ (\text{m}^2\ \text{W}^{-1}) \tag{16}$$

$$\beta = \frac{2\sqrt{2}\Delta T}{L_{\text{eff}}I_0}\ (\text{m W}^{-1}) \tag{17}$$

ΔT represents the valley value on the open aperture Z-scan curve in the above equation. For saturated absorption, β will be negative, whereas it will be positive for two-photon absorption, also known as reverse saturable absorption. At these very low intensities, the normalized transmittance of samples decreases gradually as the sample position (Z) approaches zero (focal point). The dip in the normalized transmittance curve represents the lowest feasible value of transmittance at the focal point.[56,57] A valley in the open aperture curve, as depicted in Fig. 12b, confirms the presence of strong reverse saturable absorption (RSA), as the positive nonlinear absorption of the molecule in the excited state is comparatively higher than the absorption in the ground state, which ensures the strong RSA effect. Its behavior in optical limiting, photonic, and medical applications is exemplary in this regard.

$$\text{Re}\chi^{(3)}\ (\text{esu}) = \frac{10^{-4}\varepsilon_0 c^2 {n_0}^2 n_2}{4\pi^2}\ (\text{cm}^2\ \text{W}^{-1}) \tag{18}$$

$$\text{Im}\chi^{(3)}\ (\text{esu}) = \frac{10^{-2}\varepsilon_0 c^2 {n_0}^2 \lambda\beta}{4\pi^2}\ (\text{cm W}^{-1}) \tag{19}$$

$$\chi^{(3)} = \sqrt{(\text{Re}\chi^{(3)})^2 + (\text{Im}\chi^{(3)})^2} \tag{20}$$

The comparision of ($\chi^{(3)}$) with other reported references are tabulated (Table 4).[32,58,59] The nonlinear absorption coefficient β is 1.1739×10^{-5} (cm W^{-1}). Third order nonlinear refractive index n_2 is 1.6639×10^{-12} (cm^2 W^{-1}).

In closed aperture spectrum shows the variation in valley-to-peak transmittance as a function of the linear displacement of the sample along the z-axis that demonstrates the self-focusing effect (SFE) with positive nonlinearity ($n_2 > 0$). It determines reverse saturation absorption. As a result of the overall investigations, the material under consideration may have a better NLO response in all-optical switching, optical limiting, and so on.

Table 3 Optical resolution of the Z-scan setup and third order nonlinear optical parameters of the RbHSH crystal

Parameters and notations	Details
Laser wavelength (λ)	632.8 nm
Lens focal length (f)	200 mm
Beam waist radius (ω_a)	10 mm
Aperture radius (r_a)	4 mm
Sample thickness (L)	1 mm
Nonlinear refractive index (n_2)	1.6639×10^{-12} (cm^2 W^{-1})
Nonlinear absorption coefficient (β)	1.1739×10^{-5} (cm W^{-1})
Third order nonlinear susceptibility ($\chi^{(3)}$)	4.86331×10^{-9} (esu)
Linear absorption coefficient (α)	116.55
Critical wavelength	1.027×10^{-6}
Imaginary part of the third order susceptibility [Im($\chi^{(3)}$)]	4.8613×10^{-9} (esu)
Real part of the third order susceptibility [Re($\chi^{(3)}$)]	1.3676×10^{-10} (esu)

Atomic force microscopy analysis

Atomic force microscopy analysis can be utilised to learn about the morphology of the developed surface by obtaining the surface topography. The 2D and 3D AFM pictures are shown in Fig. 13a and b. The topography data should be used to assess each line (2D) or overall profile (3D). AFM can be used to examine four critical factors: spacing, amplitude, functionality, and hybridity. Amplitude parameters are the primary parameters for characterising surface topography. The 3D image view reveals the presence of topographical features on the crystal surface, characterised by both imperfections and mountains. The software Nano surf scan version 1-4-0-3 was utilised to estimate multiple parameters, including roughness average, mean value, root-mean-square

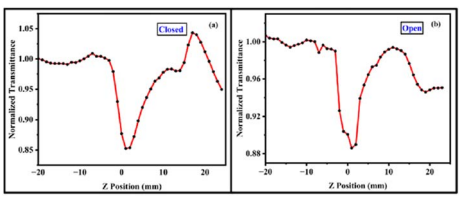

Fig. 12 (a) Z scan curve closed aperture & (b) open aperture spectrum of RbHSH crystal.

Table 4 Comparison of third order susceptibility with other crystals

Crystal	Third order susceptibility ($\chi^{(3)}$) esu	References
Potassium succinate–succinic acid	6.4649×10^{-9}	42
Potassium tri-hydrogen di-succinate	5.9056×10^{-5}	25
Sodium boro succinate	3.5×10^{-4}	43
Rubidium hydrogen succinate hydrate	4.86331×10^{-9}	Present work

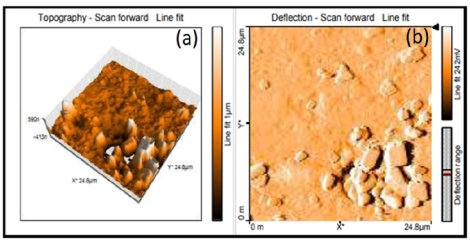

Fig. 13 (a) 3D and (b) 2D AFM images of the RbHSH crystal.

value, valley depth, peak height, and peak-valley height.[60] All the determined roughness parameters are shown in Table S8 in ESI files.† The grown RbHSH crystal surface area is measured to be 618 pm^2. Root mean square (S_q) and average roughness (S_a) are the two important amplitude parameters. Since there are many peaks and valleys in the image, it is preferred to determine the median peak-to-valley difference because this has a major impact on the S_q and S_a values. The S_q and S_a values were found to be 160.24 and 97.076 nm, respectively. The peak-valley height (S_y) of RbHSH is observed to be 2044.6 nm.

Conclusions

A transparent rubidium hydrogen succinate hydrate single crystal has been grown by the slow evaporation solution growth technique. The triclinic structure with the $P\bar{1}$ centrosymmetric space group of the compound was confirmed by SXRD. FTIR identified the presence of various functional groups of the grown RbHSH crystal. The grown crystal exhibited 89% transparency with an optical bandgap energy of 5.21 eV. The grown material is thermally stable up to 174 °C. The grown crystal exhibits low dielectric loss and dielectric constant behavior, which improves its application in device fabrication and the photonic industry. The Vickers microhardness analysis of the grown crystal showed that it belongs to the soft material category. The photoconductivity studies confirm that the material exhibits negative photoconductivity. From the PL spectrum, the blue emission peak was obtained at 484 nm. The 3D and 2D fingerprint plots of intermolecular interactions, such as O–H, O–C, Rb–H, C–C, Rb–O, H–H, O–O and H–C contacts, were examined using Hirshfeld surface analysis in the RbHSH molecule. The Z-scan approach was used to examine the third order NLO properties. The $\chi^{(3)}$ value of the RbHSH crystal is 4.86331×10^{-9} esu. The nonlinear absorption coefficient β is 1.1739×10^{-5} (cm W^{-1}) and refractive index n_2 is 1.6639×10^{-12} (cm^2 W^{-1}). Based on these findings, the high mechanical stability and high transparency value make the grown crystal a potential material in constructing high-power laser devices.

Author contributions

S. Kavitha: conceptualization, data curation, investigation, writing – original draft, methodology, formal analysis. R. Ezhil Vizhi: conceptualization, methodology, supervision, investigation, resources, visualization.

Conflicts of interest

The authors declare that they have no known competing financial interests or personal relationships that could have appeared to influence the work reported in this paper.

Acknowledgements

The authors are thankful to the management Vellore Institute of Technology, Vellore, Tamil Nadu, India for their constant support and the characterization facilities provided. The authors are very much thankful to the Single crystal XRD facility at VIT, Vellore, and Sri Sivasubramaniya Nadar College of Engineering for characterization facility of dielectric and Z scan. Authors would like to thank Ms. K. Anitha, Department of Physics, Madurai Kamaraj University, for helping crystal structure refinement.

References

1 G. Gokila, R. Aarthi and C. Ramachandra Raja, *Optik*, 2020, **206**, 164324.
2 P. Karuppasamy, D. Joseph Daniel, H. J. Kim, M. Senthil Pandian and P. Ramasamy, *J. Cryst. Growth*, 2020, **535**, 125528.
3 A. J. McGaughey, A. Jain, H. Y. Kim and B. Fu, *J. Appl. Phys.*, 2019, **125**(1), 011101.
4 K. Juliet sheela and P. Subramanian, *Phys. B Condens. Matter.*, 2018, **534**, 156–162.
5 K. Mahendra, B. J. Fernandes, J. Pattar, S. Pujar, B. S. Nagaraja, K. P. Ramesh and N. K. Udayashankar, *Mater. Sci. Eng. B Solid-State Mater. Adv. Technol.*, 2023, **288**, 116157.
6 S. Sindhusha, C. M. Padma, B. Gunasekaran and H. Marshan Robert, *J. Mol. Struct.*, 2020, **1209**, 127981.
7 N. Kalsbeek, *Acta Crystallogr. Sect. C Cryst. Struct. Commun.*, 1992, **48**, 1389–1394.

8 S. Jeeva, S. Muthu, S. Tamilselvan, M. L. Caroline, P. Purushothaman, S. Sevvanthi, G. Vinitha and G. Mani, *Chin. J. Phys.*, 2018, **56**, 1449–1466.
9 S. Anna Venus, S. Anbarasu and P. A. Devarajan, *Optik (Stuttg.)*, 2015, **126**, 4561–4565.
10 D. S. Ajisha and R. E. Vizhi, *J. Solid State Chem.*, 2021, **293**, 121642.
11 S. Vasumathi, H. J. Jeyakumar and P. Selvarajan, *J. Mol. Struct.*, 2022, **1263**, 133158.
12 A. Arunkumar and P. Ramasamy, *Mater. Lett.*, 2014, **123**, 246–249.
13 S. Das, S. Paikaray, I. Swain, S. Senapati and R. Naik, *Surf. Interfaces*, 2023, **42**, 103395.
14 S. Das, P. Priyadarshini, D. Alagarasan, S. Vardhrajperumal, R. Ganesan and R. Naik, *J. Non-Cryst. Solids*, 2022, **592**, 121742.
15 S. V. A. Santhia, B. Aneeba, S. Vinu and R. S. Christy, *J. Mater. Sci. Mater. Electron.*, 2021, **32**, 21065–21082.
16 K. Premlatha, N. R. Rajagopalan and P. Krishnamoorthy, *J. Mol. Struct.*, 2021, **1240**, 130593.
17 S. P. Rathee, D. S. Ahlawat, S. A. M. B. Dhas, K. K. Mauray, B. Singh and I. Bdikin, *Solid State Commun.*, 2020, **319**, 114010.
18 D. S. Ajisha, R. Chakaravarthy and R. E. Vizhi, *Mater. Chem. Phys.*, 2022, **283**, 125952.
19 A. Senthil and P. Ramasamy, *J. Cryst. Growth*, 2014, **401**, 200–204.
20 R. Priya, S. Anitha, P. S. L. Mageshwari and R. Ragu, *J. Mater. Sci. Mater. Electron.*, 2020, **31**, 21288–21302.
21 D. Sahoo, P. Priyadarshini, A. Aparimita, D. Alagarasan, R. Ganesan, S. Varadharajaperumal and R. Naik, *RSC Adv.*, 2020, **10**, 26675–26685.
22 R. Naik, P. P. Sahoo, C. Sripan and R. Ganesan, *Opt. Mater. (Amst.)*, 2016, **62**, 211–218.
23 R. Naik, A. Jain, R. Ganesan and K. S. Sangunni, *Thin Solid Films*, 2012, **520**, 2510–2513.
24 M. Novaković, M. Popović, K. Zhang, Z. Rakočević and N. Bibić, *Opt. Mater. (Amst.)*, 2016, **62**, 57–63.
25 Kumar, S. M. Ravi, R. Srineevasan and R. Ravisankar, Synthesis, growth, structure, optical, mechanical, and electrical properties of an Inorganic new nonlinear optical crystal: sodium manganese tetra chloride (SMTC), *IOP Conference Series: Materials Science and Engineering*, IOP Publishing, 2018, vol. 360(1).
26 K. Anitha, M. Subha and M. T. Elakkiya, *J. Mol. Struct.*, 2021, **1244**, 130850.
27 S. M. Azhar, M. Anis, S. S. Hussaini, S. Kalainathan, M. D. Shirsat and G. Rabbani, *Opt. Laser Technol.*, 2017, **87**, 11–16.
28 B. Aneeba, S. V. A. Santhia, S. Vinu, A. Baazeem and R. S. Christy, *J. King Saud Univ., Sci.*, 2021, **33**, 101443.
29 D. Sahoo, P. Priyadarshini, R. Dandela, D. Alagarasan, R. Ganesan, S. Varadharajaperumal and R. Naik, *RSC Adv.*, 2021, **11**, 16015–16025.
30 J. Beena, A. . Jebamalar, S. Sindhusha and T. Kamalesh, *Opt. Mater. (Amst.)*, 2022, **133**, 112938.
31 S. Chennakrishnan, S. M. Ravi Kumar, C. Shanthi, R. Srineevasan, T. Kubendiran, D. Sivavishnu and M. Packiya raj, *J. Taibah Univ. Sci.*, 2017, **11**, 955–965.
32 S. Anitha, P. S. Latha Mageshwari, R. Priya, R. Ragu and S. Jerome Das, *Chin. J. Phys.*, 2022, **76**, 145–171.
33 D. Nayak, N. Vijayan, M. Kumari, K. Kiran, N. Thirughanasambantham, V. Balachandran, S. Das and R. P. Pant, *Braz. J. Phys.*, 2023, **53**, 1–11.
34 S. U. Narmatha and S. R. Thilagavathy, *Mater. Today: Proc.*, 2022, **48**, 394–399.
35 S. Sathiskumar and M. Thairiyaraja, *J. Opt.*, 2022, **51**, 1052–1064.
36 D. S. Christy, X. S. Shajan and C. K. Mahadevan, *J. Phys. Sci.*, 2022, **33**, 29–49.
37 S. Suresh and K. Anand, *Int. J. ChemTech Res.*, 2013, **5**, 284–287.
38 S. Suresh and M. Priya, *Int. J. ChemTech Res.*, 2014, **6**, 5604–5607.
39 P. Saminathan, M. SenthilKumar, S. Shanmugan, P. Selvaraju, B. Janarthanan and K. K. Sadasivuni, *Mater. Today: Proc.*, 2020, **30**, 57–61.
40 S. Zhang and X. Zhang, *Thin Solid Films*, 2012, **520**, 2375–2389.
41 B. S. I. Lasalle, T. Kamalesh, P. Karuppasamy, M. S. Pandian and P. Ramasamy, *J. Mater. Sci.: Mater. Electron.*, 2022, **33**, 24718–24733.
42 A. Anbarasi, S. M. Ravi Kumar, G. J. S. Sundar, M. A. Mosses, M. P. Raj, M. Prabhakaran, R. Ravisankar and R. Gunaseelan, *Phys. B (Amsterdam, Neth.)*, 2017, **522**, 31–38.
43 D. Alagarasan, S. Varadharajaperumal, K. D. A. Kumar, R. Naik, S. Umrao, M. Shkir, S. AIFaify and R. Ganesan, *Opt. Mater. (Amst.)*, 2021, **121**, 111489.
44 M. Parthasarathy, S. Mani Naidu, P. Chinna Babu, B. Gowri Shannkari, M. Krishnakumar, V. R. M. Reddy, W. K. Kim, S. Mohd and I. M. Ashraf, *J. Mater. Sci. Mater. Electron.*, 2023, **34**, 1–18.
45 A. Ali, Z. U. Din, M. Ibrahim, M. Ashfaq, S. Muhammad, D. Gull, M. N. Tahir, E. Rodrigues-Filho, A. G. Al-Sehemi and M. Suleman, *RSC Adv.*, 2023, **13**, 4476–4494.
46 J. Dalal and B. Kumar, *Opt. Mater. (Amst.)*, 2016, **51**, 139–147.
47 S. Chinnasami, P. Rajesh, R. Bhatt, I. Bhaumik, P. Ramasamy and A. K. Karnal, *Chin. J. Phys.*, 2020, **67**, 135–146.
48 G. E. Robin, U. Sankar, T. Chithambarathanu and P. Selvarajan, *Int. J. Adv. Sci. Tech. Res.*, 2014, **6**, 284–294.
49 S. Chandran, R. Paulraj, P. Ramasamy and K. K. Maurya, *J. Inorg. Organomet. Polym. Mater.*, 2017, **27**, 1383–1390.
50 A. C. Sajikumar, *Int. J. Phys. Appl.*, 2016, **8**, 53–57.
51 S. Goel, N. Sinha, H. Yadav, A. J. Joseph, A. Hussain and B. Kumar, *Arab. J. Chem.*, 2020, **13**, 146–159.
52 S. Das, D. Alagarasan, S. Varadharajaperumal, R. Ganesan and R. Naik, *Mater. Adv.*, 2022, **3**, 7640–7654.
53 A. H. Al-Hamdani, *Int. J. Nanoelectron. Mater.*, 2013, **6**, 139–146.
54 M. Ebrahimi Naghani, M. Neghabi, M. Zadsar and H. Abbastabar Ahangar, *Sci. Rep.*, 2023, **13**, 1–10.

55 P. Priyadarshini, S. Das, D. Alagarasan, R. Ganesan, S. Varadharajaperumal and R. Naik, *Sci. Rep.*, 2021, **11**, 1–13.
56 A. Aparimita, P. Khan, J. R. Aswin, K. V. Adarsh and R. Naik, *J. Appl. Phys.*, 2020, **127**(7), 075102.
57 A. Dilli Rani, M. Nageshwari, C. Rathika Thaya Kumari, P. Ramesh, P. Sangeetha, G. Vinitha, M. Lydia Caroline and S. Kumaresan, *J. Mater. Sci. Mater. Electron.*, 2023, **34**, 1–18.
58 A. Arunkumar, P. Ramasamy, K. Vishnu and M. K. Jayaraj, *J. Mater. Sci.*, 2014, **49**, 3598–3607.
59 A. Vijayalakshmi and B. Vidyavathy, *UPB Sci. Bull. Ser. B Chem. Mater. Sci.*, 2017, **79**, 221–231.
60 R. Hanumantharao and S. Kalainathan, *J. Chem.*, 2013, **2013**, 305932.